Toughening in Graphene Ceramic Composites

Luke S. Walker,[†] Victoria R. Marotto,[†] Mohammad A. Rafiee,[‡] Nikhil Koratkar,[‡] and Erica L. Corral[†,*]

[†]Materials Science and Engineering Department, University of Arizona, Tucson, Arizona 85748, United States, and [‡]Department of Mechanical, Aerospace and Nuclear Engineering, Rensselaer Polytechnic Institute, Troy, New York 12180, United States

ABSTRACT The majority of work in graphene nanocomposites has focused on polymer matrices. Here we report for the first time the use of graphene to enhance the toughness of bulk silicon nitride ceramics. Ceramics are ideally suited for high-temperature applications but suffer from poor toughness. Our approach uses graphene platelets (GPL) that are homogeneously dispersed with silicon nitride particles and densified, at ~1650 °C, using spark plasma sintering. The sintering parameters are selected to enable the GPL to survive the harsh processing environment, as confirmed by Raman spectroscopy. We find that the ceramic's fracture toughness increases by up to ~235% (from ~2.8 to ~6.6 MPa·$m^{1/2}$) at ~1.5% GPL volume fraction. Most interestingly, novel toughening mechanisms were observed that show GPL wrapping and anchoring themselves around individual ceramic grains to resist sheet pullout. The resulting cage-like graphene structures that encapsulate the individual grains were observed to deflect propagating cracks in not just two but three dimensions.

KEYWORDS: ceramics · silicon nitride · graphene · nanocomposites · fracture toughness

Graphene with its combination of large specific surface area, two-dimensional high aspect ratio sheet geometry, and outstanding mechanical properties[1−5] shows great promise as a nanofiller in composite materials. A number of studies with polymer-based matrices[6−11] have demonstrated that graphene fillers can significantly improve the mechanical properties of polymers at relatively low nanofiller loading. However, to our knowledge, there is no report so far on the use of graphene additives to improve the mechanical properties of bulk ceramics. Structural ceramics are becoming increasingly relevant for high-temperature applications.[12] In particular, silicon nitride (Si_3N_4) is a high-temperature-resistant ceramic (up to 1500 °C) and is also considered the most reliable structural ceramic due to the formation of an interlocking microstructure of α-Si_3N_4 that is reinforced with long rod-like β-Si_3N_4 grains.[12] This self-reinforced microstructure results in a high resistance to fracture due to the β-Si_3N_4 grains and high hardness due to the matrix of α-Si_3N_4 grains.[12] The combination of high hardness and toughness in one material composition and the ability to tailor each property based on the microstructure is the principal reason why Si_3N_4 is considered the leading structural ceramic. However, Si_3N_4 is still not widely used in many elevated temperature (>1000 °C) applications due to its overall low toughness properties in comparison to metals.

Conventional ceramic matrix composites (CMCs) use one-dimensional fibers as the reinforcement phase, such as carbon fibers[13] or carbon nanotubes[14,15] and ceramic whiskers.[16,17] To the best of our knowledge, there are currently no reports showing CMCs processed with graphene reinforcement for mechanical property enhancement. A major reason why processing graphene reinforced bulk ceramic composites has been limited is the thermal stability limitations of graphene at high temperature. Ceramics start to densify and sinter at temperatures >1000 °C, and Si_3N_4 is usually sintered at ~1800 °C, therefore making it challenging to incorporate graphene which has low thermal stability at temperatures in excess of ~600 °C.[18] In order to determine the true effect of graphene on the toughness of Si_3N_4 and to eliminate the effect of the β-Si_3N_4 grains on toughening, we chose to control the matrix microstructure to be approximately 100% α-Si_3N_4 (equiax grains). We did so using spark plasma sintering (SPS), which is a process that reduces the time at temperature from hours to minutes over conventional sintering methods, thus allowing accurate control of the α- to β-Si_3N_4 conversion, and also limits thermally induced structural damage to the graphene platelets (GPL) by avoiding long processing times at high temperature.

RESULTS AND DISCUSSION

In order to obtain uniform, densified microstructures of our nanocomposites, we used colloidal processing methods to create homogenously dispersed particle

* Address correspondence to elcorral@email.arizona.edu.

Received for review January 25, 2011 and accepted March 28, 2011.

Published online March 28, 2011
10.1021/nn200319d

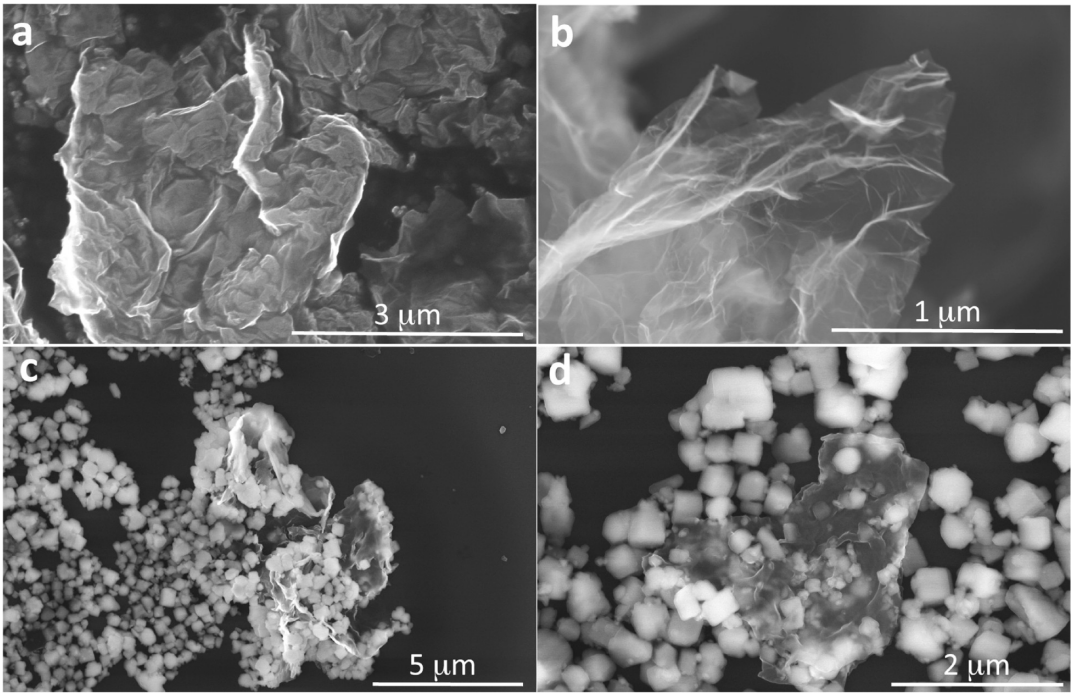

Figure 1. GPL and GPL-Si_3N_4 powder particles. (a) Low- and (b) high-resolution SEM images of as-produced graphene platelets showing tightly packed platelets containing crumpled sheets of graphene. (c) Low- and (d) high-resolution SEM images after colloidal processing indicating partially exfoliated GPL mixed with well-dispersed Si_3N_4 particles. The images clearly indicate GPL decorated with Si_3N_4 particles; the Si_3N_4 particles are well-dispersed throughout the surface area of the sheets.

systems in aqueous suspension.[19−22] Highly dispersed GPL/Si_3N_4 nanocomposite slurries, using 0.02, 0.5, 1.0, and 1.5 vol % graphene (total solids basis), were processed using methods based on our previous work with single-walled carbon nanotube (SWNT)-Si_3N_4 ceramic nanocomposites.[23] Bulk quantities of GPL used in this study were produced by the rapid thermal expansion (>2000 °C min^{-1}) of graphite oxide.[24,25] The platelets comprised on average of ∼3−4 graphene sheets with less than 2 nm thickness.[25] Elemental analysis gave the carbon to oxygen ratio in GPL as ∼9.1 to 1, which confirmed that the majority of oxygen-containing moieties were expelled due to the thermal shock. Figure 1a,b shows typical scanning electron microscopy (SEM) images of the as-produced GPL. The GPLs are agglomerated, as seen in Figure 1a, before the colloidal processing step. In Figure 1b, the higher resolution SEM image shows the wrinkled surface of a few partially separated graphene sheets.

We have previously shown that the dispersion of SWNTs using a cationic surfactant, cetyltrimethylammonium bromide (CTAB), occurs because the hydrophobic SWNTs are attracted to the hydrophobic tails of the surfactant, resulting in SWNTs that are covered in positively charged surfactant molecules.[23,26] We used CTAB as the dispersant throughout this study to disperse GPLs, assuming a carbon surface chemistry similar to that of the SWNTs. The amount of surfactant used was based on its dry weight and was used at a concentration above the critical micelle concentration. We used 1.0 wt % CTAB to GPLs and 1.0 wt % CTAB to Si_3N_4 powders in order to create a positive electrostatic repulsive force between the two phases of the composite materials and with each other. This electrostatic repulsion was developed due to the net charge from the positive headgroup on the surfactant molecules on the graphene platelets and the Si_3N_4 particles. Panels c and d of Figure 1 show SEM images of the GPL and Si_3N_4 powder mixtures after aqueous colloidal processing. Figure 1c shows GPLs separated from each other among a uniform dispersion of Si_3N_4 particles. Figure 1d shows a higher resolution image of a GPL decorated with individual Si_3N_4 particles, which are also enveloped within the GPL.

SPS is a relatively new high-temperature powder consolidation method that has already been used to successfully create fully dense ceramics,[27−29] nanoceramics,[30,31] and ceramic nanocomposites reinforced with carbon nanotubes.[23,32−35] The advantages of using SPS to densify ceramics are (1) rapid heating rates (up to 600 °C/min) and (2) simultaneous applied pressure (60−120 MPa). SPS simultaneously applies pressure and quickly pulses electric current through a graphite die containing the ceramic powders that are to be densified. The pulsed current assists in densification upon applied pressure and relies on creep and related mechanisms for densification and not the conventional sintering methods that involve diffusion and mass transport of material across the grain boundaries during long periods of time at elevated

TABLE 1. Physical Properties of Si_3N_4 Monoliths Densified Using SPS

starting material composition	SPS heating rate (°C/min)	sintering temperature (°C)	hold time (min)	applied load (MPa)	% theoretical density	final material composition
α-Si_3N_4	100	1500	5	35	87.6	100% α-Si_3N_4
α-Si_3N_4	100	1575	5	35	98.4	100% α-Si_3N_4
α-Si_3N_4	100	1600	5	35	99.5	100% α-Si_3N_4
α-Si_3N_4	100	1700	5	35	99.0	83% α-Si_3N_4
α-Si_3N_4	100	1600	2	35	93.8	>99% α-Si_3N_4
α-Si_3N_4	100	1625	2	35	97.0	>99% α-Si_3N_4
α-Si_3N_4	100	1650	2	35	100.0	>99% α-Si_3N_4

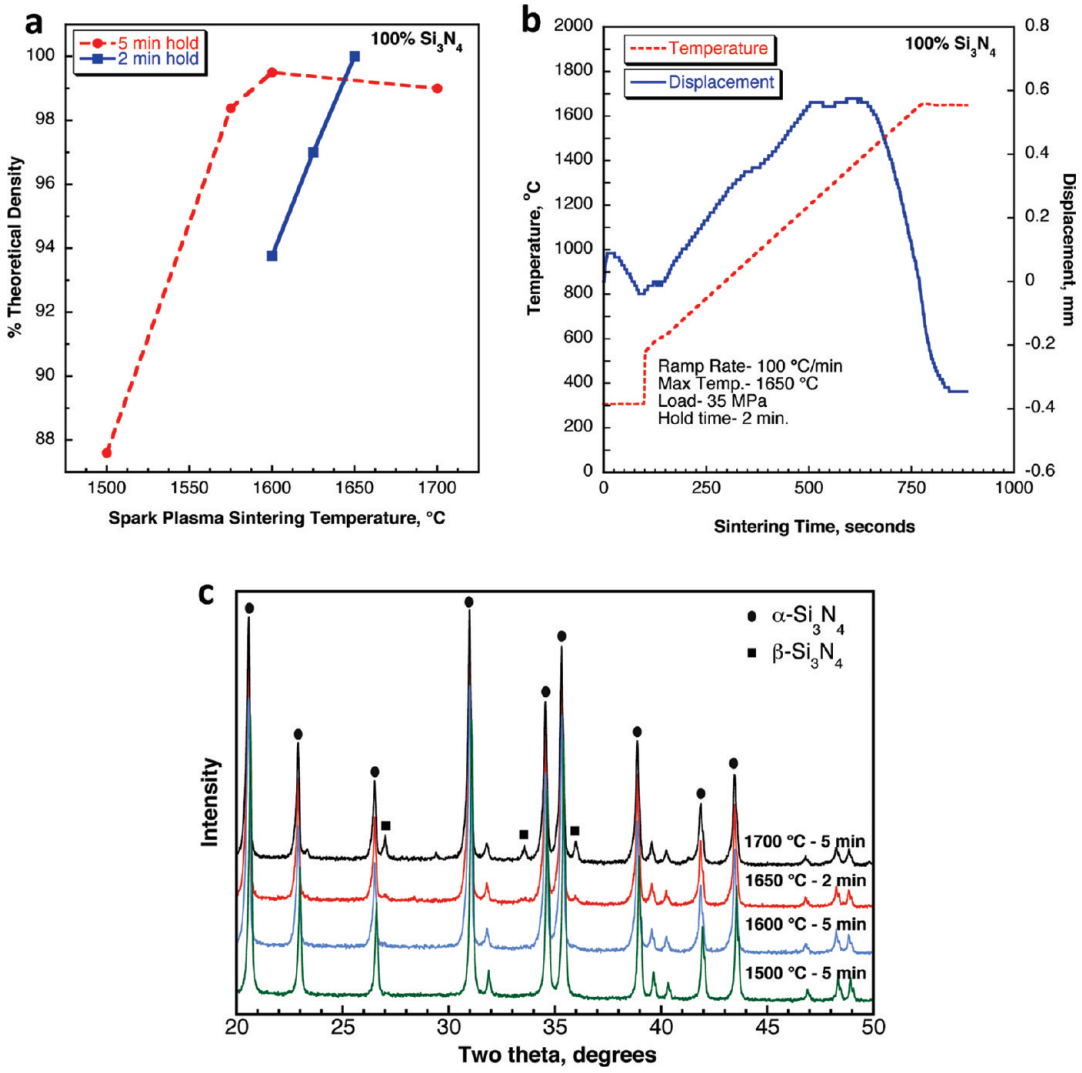

Figure 2. Spark plasma sintering of Si_3N_4 matrix material. (a) Density of Si_3N_4 is plotted as a function of sintering temperature for two different times at temperature which are 5 min hold and 2 min hold at temperature; 100% of theoretical density for the matrix material is obtained at ~1650 °C, for 2 min hold at temperature. (b) Densification profile for this high-density part shows a steady increase in displacement with increasing temperature up to the final sintering temperature. (c) X-ray diffraction phase analysis of the matrix after SPS shows that for the highest density part (1650 °C) we retain a phase composition that is approximately 100% α-Si_3N_4.

temperatures.[28] For this study, we used SPS to densify our nanocomposite powders with precise control of the matrix microstructure and to limit the time at temperature to minimize the possibility of structural damage to the GPL at high temperatures and pressures. The protocols used for SPS operation and nancomposite and graphene preparation are provided in the Materials and Methods section.

Table 1 shows the SPS heating rate, time at temperature, hold time, percent theoretical density (% TD), and final material composition obtained for monolithic Si_3N_4. The goal of this preliminary densification investigation

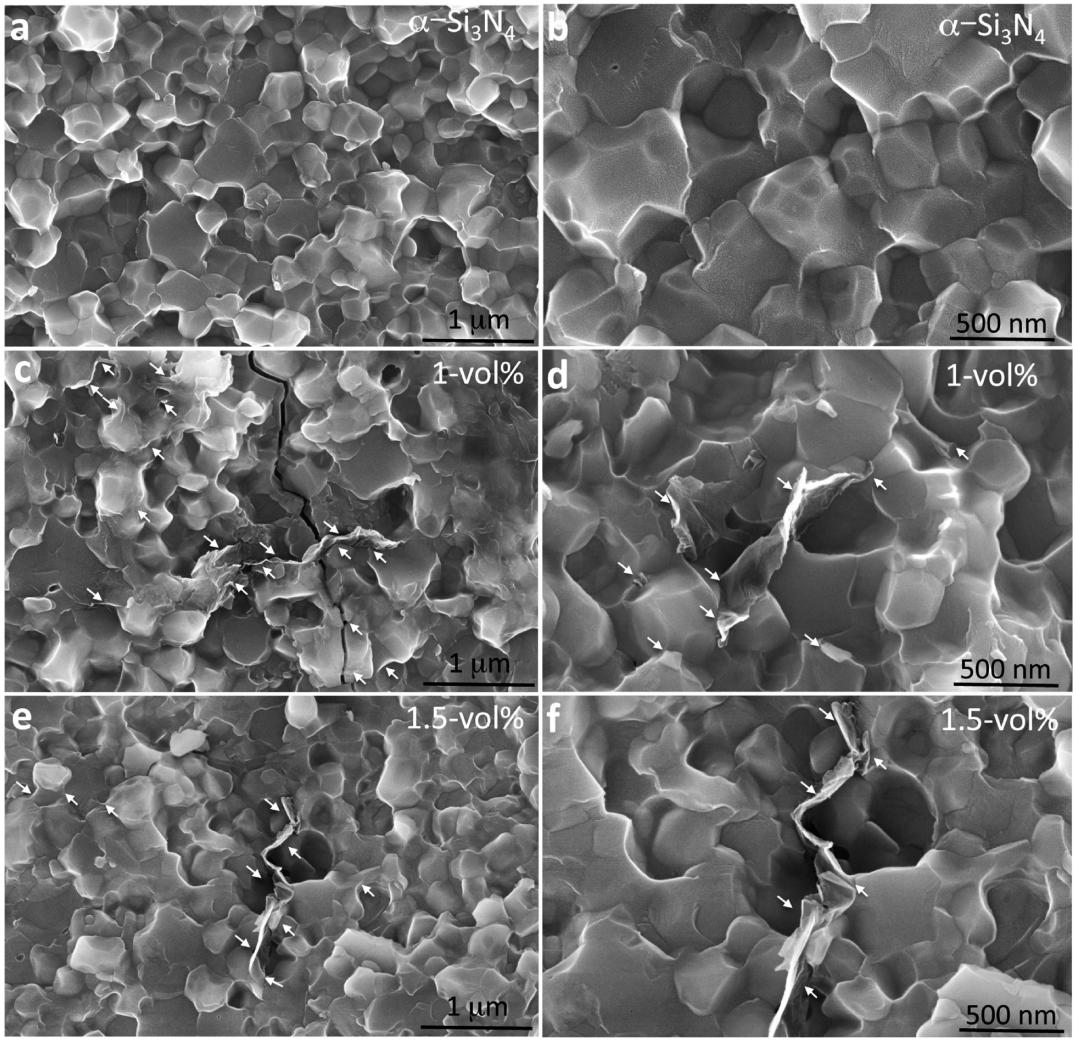

Figure 3. SEM fracture surface images of Si_3N_4 and GPL nanocomposites. (a) Low- and (b) higher-magnification SEM images of the high-density 100% α-Si_3N_4 monolithic ceramic matrix material showing an equiaxed and homogeneous grain microstructure. (c) Low- and (d) higher-magnification SEM images of the sintered and fractured 1.0 vol % GPL-Si_3N_4 nanocomposite. The small white arrows illustrate the location of GPL on the fracture surface image. The large crack running through image c indicates the presence of GPL along the grain boundary of the matrix material. Corresponding (e) low- and (f) high-magnification SEM images of the 1.5 vol % GPL-Si_3N_4 nanocomposite.

was to determine the SPS parameters that would result in creating nearly 100% α-Si_3N_4 while maintaining high density at the lowest possible temperature and shortest amount of time at temperature. Figure 2a shows the density plot for monolithic Si_3N_4 sintered from 1500 to 1700 °C, using two different hold times of 2 and 5 min at temperature. The 5 min density plot shows that the density increases with increasing temperature from 1500 to 1600 °C (99.5% TD) and then remains relatively constant up to ~1700 °C (99.0% TD). The 2 min density plot shows that the effect of temperature on densification is significantly greater when using a shorter hold time (keeping the heating rate constant) and results in 100% TD at ~1650 °C. Figure 2b shows the shrinkage displacement curve and the heating profile curve that was measured during the SPS run for the high-density monolithic part sintered at ~1650 °C for 2 min. The displacement curve shows steady shrinkage displacement with increasing temperature up to ~1650 °C, which represents ideal densification behavior. Figure 2c shows the X-ray diffraction (XRD, X'Pert MPD Pro, PANalytical, Westborough, MA, USA) (Cu Kα) patterns for the monoliths sintered at various temperatures and hold times. Specifically, the XRD spectrum for the monolith sintered at 1650 °C, for only 2 min, confirms that SPS can be used to tailor the matrix microstructure to ~100% α-Si_3N_4 while achieving high density. The accurate and reliable control of the matrix microstructure (α-Si_3N_4) is important because we want to evaluate the effect of GPL as structural reinforcement within a uniform and homogeneous equiax grain matrix microstructure. The XRD spectra for the monoliths sintered at 1500, 1600, and 1700 °C for 5 min at temperature are also shown in Figure 2c with the percentage of each phase listed in Table 1. As expected, the phase content transitions from 100% α-Si_3N_4 to β-Si_3N_4 formation with increasing sintering temperature.

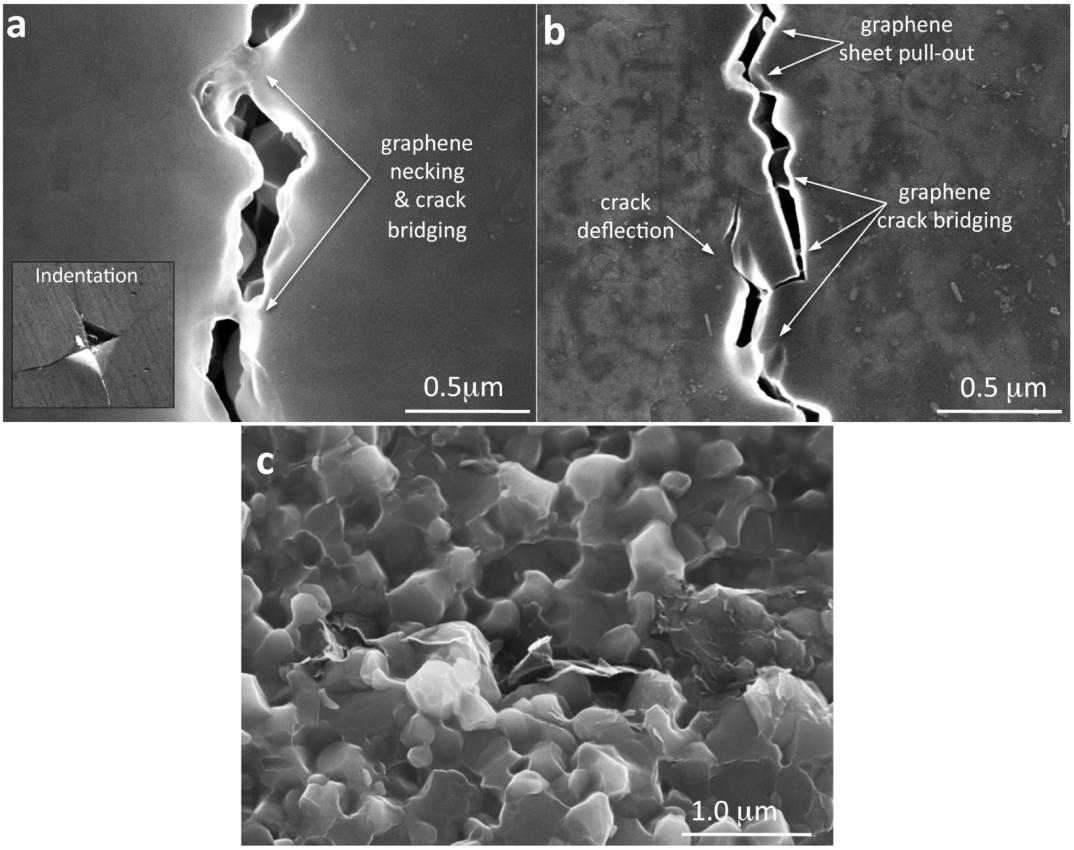

Figure 4. Toughening mechanisms in GPL-Si_3N_4 nanocomposites. (a) Microhardness testing resulting in the creation of radial cracks stemming from the microhardness indent (inset image). Closer examination of the radial cracks reveals GPL bridging the crack at several locations, two of which are shown in this high-resolution SEM image. (b) Further examination of the radial cracks indicates that they follow a tortuous crack propagation path. (c) Fracture surface of the bulk sample indicates the presence of three-dimensional toughening mechanisms for the GPL-Si_3N_4 nanocomposite.

Figure 3a,b shows SEM images of two different fracture surfaces for the same specimen of ~100% α-Si_3N_4 (>99% TD). The grain size is estimated as ~500 nm, and the grains are uniform throughout the fracture surfaces. Figure 3c,d shows SEM images of two different fracture surfaces for the same 1.0 vol % GPL-Si_3N_4 nanocomposite. Figure 3c is the lower resolution image showing the α-Si_3N_4 grain matrix microstructure. It also indicates homogeneous dispersion of the GPL throughout the nanocomposite (as pointed out by the small white arrows directly labeled on the image). This specific image (Figure 3c) was taken at this area because of the interesting interactions between the large crack that runs through the bulk of the specimen and the GPL at the center of the image. First, we notice that the GPL is protruding out of the fracture surface and it is a large platelet that runs along the grain boundaries of the matrix. The long continuous platelet of graphene does not appear to deflect the crack propagation path in-plane. However, the crack does not penetrate or puncture through the graphene platelet either. Therefore, we believe that the crack is arrested at the GPL and has to change directions (*i.e.*, undergo out-of-plane deflection) to negotiate the GPL. Thus it appears that the GPLs (which are anchored at the grain boundaries) prevent cracks from changing their propagation paths in the conventional two-dimensional spaces and force such cracks to propagate in three-dimensional space. Such a fracture resistance mechanism has hitherto not been reported in conventional CMC systems. Figure 3d is an SEM image of a fracture surface at a different location of the same nanocomposite (1.0 vol % GPL-Si_3N_4) and shows how the GPL (at the center of the image) is anchored securely within the grain boundaries of the matrix microstructure. The image also depicts smaller GPL dispersed throughout the microstructure of the nanocomposite (pointed out by the small white arrows directly labeled onto the image). In comparison with the monolith (Figure 3b), the nanocomposite microstructure is less angular and appears to exhibit less of a brittle fracture microstructure.

Figure 3e,f shows SEM images of the same fracture surface for the 1.5 vol % GPL-Si_3N_4 nanocomposite. The bulk fracture surface is similar to the 1.0 vol % GPL-Si_3N_4 nanocomposite. At lower magnification (Figure 3e), one can clearly see the graphene sheets pulled out of the fracture surface, and in other regions, they create a single layer (or possible few layers) veil of graphene that drapes over the fracture surface (top left

corner), which makes them difficult to distinguish at first glance. The higher resolution SEM image in Figure 3f illustrates a wall of graphene sheets that follows the grain boundaries of the matrix. Conventional fiber-reinforced ceramic toughening mechanisms, such as fiber pull-out, are commonly observed on fracture surfaces of bulk CMCs. For our system also, we do observe the pull-out of the graphene sheets that are tucked and wrapped around the matrix grains. We expect that the energy required to pull out a sheet is greater than that of a fiber due to "sheet wrapping" around the matrix grain boundaries and the increased contact area with the matrix.

In order to study the effect of graphene concentration on the toughness of the ceramic, we used microhardness testing to induce radial cracking from the corners of the indentation. These cracks are then measured in length in order to calculate a toughness value by using the Anstis equation[36] (eq 1). This equation uses the measured hardness (H), applied load (P), modulus (E = 300 GPa, as measured previously for Si_3N_4), crack length (c_o), and a constant for Vickers produced radial cracks in brittle ceramics (0.16) to calculate a toughness value.

$$K_C = 0.16\left(\frac{E}{H}\right)^{1/2}\left(\frac{P}{c_o^{3/2}}\right) \quad (1)$$

The Vickers hardness number (H) used to calculate the toughness values was measured using an applied load of 9.8 N in order to avoid forming radial cracks. An applied load of 98 N was used to create reproducible radial cracks that were used to measure crack values (c_o) used in eq 1. The advantage of the microindentation fracture technique is the relatively small amount of graphene needed in comparison to processing large scale specimens needed for testing using conventional ASTM methods. Note that, while microindentation is not a general method that gives accurate results for all categories of ceramics, it has been shown[36] that specifically for Si_3N_4 the microindentation technique gives reliable results. In this study, we have used this method on a comparative basis to demonstrate the impact of the addition of GPL on the fracture toughness of Si_3N_4 nanocomposites.

Figure 4a shows a representative microhardness indentation (inset image) of the 1.0 vol % GPL-Si_3N_4 nanocomposite. The area of the indent is approximately 150 μm^2 and was created using a 196 N applied load. Figure 4a,b shows high-resolution images of the microhardness induced radial cracks. Figure 4a shows crack deflection resulting in a branched crack structure. Probing within the cracks (Figure 4a,b), one can see direct evidence of "sheet pull-out" and graphene sheets that are bridging the cracks, which are directly labeled on the images. Figure 4a also shows two regions within the crack where it appears that the GPLs are necking down to a smaller cross-sectional area

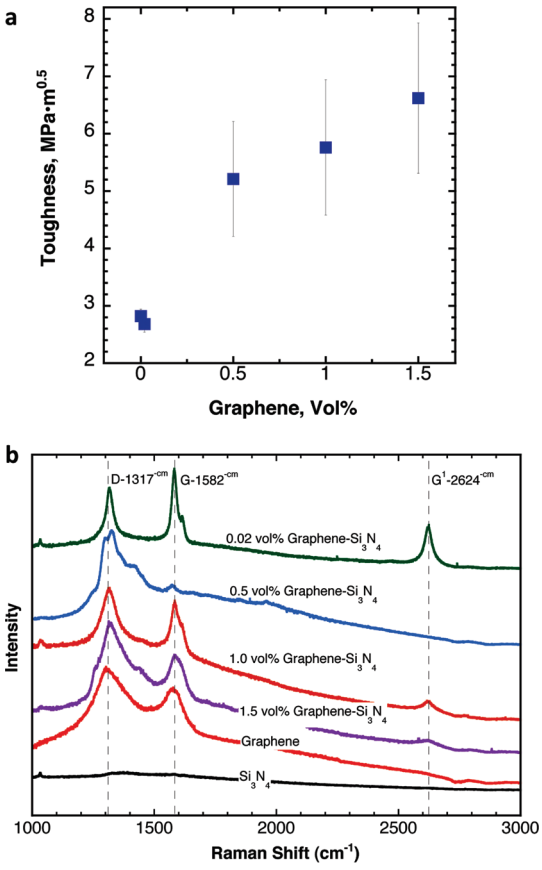

Figure 5. Toughness characterization and Raman spectra for GPL-Si_3N_4 composites. (a) Toughness of the monolith systematically increases with increasing GPL vol % from 0 to 1.5 vol % GPL. The toughness of the monolith is enhanced by ~235% using ~1.5 vol % GPL. (b) Raman spectroscopy was used to characterize the structure of the GPLs within the Si_3N_4 after SPS high-temperature densification (1650 °C for 2 min). Raman spectroscopy of the as-produced graphene shows the starting material as platelets and that the as-received starting powder of Si_3N_4 is not Raman active. At 0.02 vol % GPL, the SPS induces a transformation of the multilayer GPLs into few or bilayer graphene, which is detected by the appearance of a new peak (G′ band) at ~2624 cm^{-1}. At 0.5 vol % GPL, Raman signature of nanodiamonds is observed, while at 1.0 and 1.5 vol % GPL, we detect a mixture of few-layered and multilayer graphene.

within the crack wake. Figure 4c shows the bulk fracture surface for the 1.0 vol % GPL-Si_3N_4 nanocomposite. The GPL at the center of the image is protruding out of the surface and follows the contours formed by the matrix grain boundaries. This fracture surface again illustrates the ability of the GPL to block the in-plane propagation of the crack, thereby forcing it to climb over the wall of graphene sheets. Such a fracture surface is unexpected for a ceramic and suggests that the two-dimensional GPL promotes the deflection of cracks in three dimensions.

Figure 5a is a plot of the calculated toughness values for the GPL-Si_3N_4 nanocomposites, shown as a function of GPL concentration from 0, 0.02, 0.5, 1.0, and 1.5 vol % GPL. The plot shows a systematic increase in toughness with increasing GPL concentration from ~2.8

TABLE 2. Physical and Mechanical Properties of GPL-Si_3N_4 Nanocomposites

starting material composition	density (g/cm^3)	% theoretical density	hardness (GPa)	toughness (MPa·m$^{1/2}$)
0.00 vol % GPL + 100.00 vol % Si_3N_4	3.223	100.0	22.3 ± 0.84	2.8 ± 0.12
0.02 vol % GPL + 99.98 vol % Si_3N_4	3.204	99.5	21.2 ± 0.34	2.7 ± 0.14
0.50 vol % GPL + 99.50 vol % Si_3N_4	3.198	99.7	19.3 ± 0.69	5.21 ± 1.00
1.00 vol % GPL + 99.00 vol % Si_3N_4	3.175	99.3	20.4 ± 0.37	5.8 ± 1.18
1.50 vol % GPL + 98.50 vol % Si_3N_4	3.175	99.6	15.7 ± 0.61	6.6 ± 1.31

to ~6.6 MPa·m$^{1/2}$. The increase in toughness over the monolith is as high as ~235% (*i.e.*, 3-fold increase in toughness for the 1.5 vol % GPL-Si_3N_4 nanocomposite over the monolith). The performance of GPL is superior to single-walled carbon nanotube (SWNT) additives at the same filler volume fraction. For example, in ref 23, we reported fracture toughness of ~4.71 MPa·m$^{1/2}$ for a 1.0 vol % SWNT-Si_3N_4 composite, which is significantly lower than the values reported here (~5.8 MPa·m$^{1/2}$) for GPL. Fractography analysis (Figures 3 and 4) indicates the presence of a variety of toughening mechanisms for GPL, including sheet wrapping, sheet pull-out, two- and three-dimensional crack deflection, and crack bridging. Table 2 summarizes the density, theoretical density, hardness, and toughness values for each nanocomposite (0.02, 0.2, 1.0, and 1.5 vol % GPL-Si_3N_4) and the monolith that were all sintered at ~1650 °C (for 2 min).

Raman study was also performed to confirm that the sheet-like structures observed in Figures 3 and 4 are GPL. Figure 5b shows a collection of individual Raman spectra for as-produced graphene, Si_3N_4 (after sintering), and 0.02, 0.5, 1.0, and 1.5 vol % GPL-Si_3N_4 nanocomposites (after sintering). The as-received graphene shows two clear peaks at ~1317 cm^{-1} (D band) and ~1582 cm^{-1} (G band); note that the G′ peak at ~2624 cm^{-1} is absent, which is typical of multilayer sheets or platelet configuration of graphene.[37] At ~0.02 vol % of graphene in the ceramic, the Raman signature after SPS indicates a new peak at ~2624 cm^{-1} for the G′ (or 2D band). This indicates the thinning of the multilayer graphene platelets into few-layer or possibly bilayer graphene. Therefore, the high temperatures and pressures associated with SPS can transform the structure of graphene from multilayers into few-layered graphene. However, as we increase the concentration from 0.02 to 1 and 1.5 vol % GPL, the intensity of the G′ peak diminishes, suggesting that the graphene platelets are no longer being thinned as effectively at the higher loading fractions. Another interesting observation is that the Raman signature for the ~0.5 vol % GPL composite showed no peaks for the G and G′ bands. Instead a new peak at ~1332 cm^{-1} appears corresponding to crystalline diamond. Clearly, further investigation is warranted to understand the effect of spark plasma sintering (*i.e.*, pulsing direct current while under simultaneous pressure) on the thinning of GPL and the possible conversion of GPL to nanodiamonds.

CONCLUSION

To summarize, we used aqueous colloidal processing methods to obtain uniform and homogeneous dispersions of GPL and Si_3N_4 ceramic particles prior to densification using SPS. After densification at ~1650 °C, we found direct evidence of graphene in the nanocomposites using Raman spectroscopy. The only exception was ~0.5 vol % of graphene, for which case we found that the graphene was possibly converted into the nanodiamond phase. At lower concentrations (0.02 vol % GPL), we converted the GPL into thinner bilayer or few-layered graphene sheets using SPS. We measured a ~235% increase in toughness for the nanocomposite over the monolith using only 1.5 vol % addition of graphene. The SPS parameters were adjusted to ensure that we maintained the same matrix microstructure phase composition and high density (100% α-Si_3N_4 with >99% TD) for all samples. Most interestingly, we observed some very unexpected toughening mechanisms on the fracture surfaces of the nanocomposites. The GPLs appear to be anchored or wrapped underneath the matrix grains and result in the formation of a continuous wall of graphene along the grain boundaries that arrests and forces cracks to propagate in not just two but in three dimensions in order to continue to propagate through the material. Such fracture behavior in ceramics has hitherto not been reported. Graphene nanofiller reinforcement could potentially be used to enhance toughness for a range of ceramic materials enabling their widespread use in high-performance structural applications.

MATERIALS AND METHODS

Nanocomposite Powder Preparation. Cetyltrimethylammonium bromide (CTAB) was procured from Sigma-Aldrich Corp., St. Louis, MO. Si_3N_4 powders with mean particle size of ~0.77 μm measured by X-ray absorption/sedimentation technique and average surface area of ~7.7 m^2/g measured by standard BET N_2 adsorption was obtained from GS-44, Allied Signal Inc., Torrance, CA. Appropriate amounts of graphene and Si_3N_4 powder were added to separate containers of DI water with C_{16}TAB

predissolved, and the pH was adjusted to ~4 using nitric acid. The graphene and Si_3N_4 solutions were sonicated for 40 and 20 min, respectively, at 22 W using a horn sonicator, Misonix S-4000, Qsonica LLC, Newtown, CT. The dispersed solutions were then combined and sonicated for an additional 10 min (22 W) before ball milling for 24 h using alumina media. After processing, the water was evaporated at ~100 °C, and the dried nanocomposite slurries were heat treated in argon to remove the surfactant using a heating rate of ~5 °C/min up to ~500 °C for 1 h hold time.

Graphene Preparation. Graphite oxide was prepared by oxidizing graphite flakes (average diameter of ~48 μm) in a solution of concentrated sulfuric acid (95–98%), concentrated nitric acid (68%), hydrochloric acid (36–38%), and potassium chlorate (99.5%) for 96 h.[24,25] Thermal reduction of graphite oxide into graphene platelets was achieved by placing the graphite oxide powder (200 mg) in a 200 mm inner diameter, 1 m long quartz tube that was sealed at one end. The other end of the quartz tube was closed using a rubber stopper. An argon inlet was then inserted through the rubber stopper. The sample was flushed with argon for ~10 min, and the quartz tube was quickly inserted into a tube furnace (Thermolyne 79300, Thermo Fisher Scientific Inc., USA) preheated to ~1050 °C and held in the furnace for ~35 s.

Spark Plasma Sintering (SPS). The SPS apparatus (SPS 10-3, Thermal Technology, Santa Rosa, CA, USA) used in this study was operated using a max pulse current of 3000 A and max pulse voltage of 10 V. The pulse cycle was 25 ms on and 5 ms off using a heating rate of 100 °C/min. An external pressure of 35 MPa was applied from the 5 MPa preload at 20 MPa/min to the warm-up temperature of 600 °C (767A). The powders were heated inside a graphite die that was lined with graphite foil in order to prevent reactions with the die case. The control temperature was monitored using a single-color optical pyrometer that was focused to within ~6 mm of the powder sample within the die. A secondary temperature measurement was conducted using a Mo sheath type C thermocouple located in the lower punch, ~4 mm, from the bottom of the powder sample. The punch temperature was higher than the die temperature by a measured difference of 100–150 °C at the target densification temperature. A vacuum of at least ~3 Pa was achieved before application of power. After sintering, the power is shut off at and pressure held at ~35 MPa for 5 min while the furnace cools naturally at ~300 °C/min. Density values were measured using the Archimedes method. The rule of mixtures was used to calculate the nanocomposite densities, based on volume fraction, using density values of ~1.0 and ~3.22 g/cm^2 for GPL and Si_3N_4, respectively.

Acknowledgment. E.L.C. acknowledges funding support from the State of Arizona. N.K. acknowledges funding support from the U.S. Office of Naval Research (Award Number N000140910928) and the U.S. National Science Foundation (Award Number 0900188).

REFERENCES AND NOTES

1. Yu, A.; Ramesh, P.; Sun, X.; Bekyarova, E.; Itkis, M. E.; Haddon, R. C. Enhanced Thermal Conductivity in a Hybrid Graphite Nanoplatelet–Carbon Nanotube Filler for Epoxy Composites. *Adv. Mater.* **2008,** *24*, 4740–4744.
2. Lee, C.; Wei, X.; Kysar, J. W.; Hone, J. Measurement of the Elastic Properties and Intrinsic Strength of Monolayer Graphene. *Science* **2008,** *321*, 385–388.
3. Wang, X.; Zhi, L.; Müllen, K. Transparent, Conductive Graphene Electrodes for Dye-Sensitized Solar Cells. *Nano Lett.* **2008,** *8*, 323–327.
4. Balandin, A. A.; Ghosh, S.; Bao, W.; Calizo, I. Superior Thermal Conductivity of Single-Layer Graphene. *Nano Lett.* **2008,** *8*, 902–907.
5. Rafiee, M. A.; Lu, W.; Thomas, A. V.; Zandiatashbar, A; Rafiee, J.; Tour, J. M.; Koratkar, N. Graphene Nanoribbon Composites. *ACS Nano* **2010,** *4*, 7415–7420.
6. Watcharotone, S.; Dikin, A. D.; Stankovich, S.; Piner, R.; Jung, I.; Dommett, G. H. B.; Evmenenko, G.; Wu, S.; Chen, S.; Liu, C.; *et al.* Graphene–Silica Composite Thin Films as Transparent Conductors. *Nano Lett.* **2007,** *7*, 1888–1892.
7. Khan, U.; May, P.; O'Neill, A.; Coleman, J. N. Development of Stiff, Strong, Yet Tough Composites by the Addition of Solvent Exfoliated Graphene to Polyurethane. *Carbon* **2010,** *48*, 4035–4041.
8. Rafiee, M. A.; Rafiee, J.; Wang, Z.; Song, H.; Yu, Z. Z.; Koratkar, N. Enhanced Mechanical Properties of Nanocomposites at Low Graphene Content. *ACS Nano* **2009,** *3*, 3884–3890.
9. Rafiee, M. A.; Rafiee, J.; Srivastava, I.; Wang, Z.; Song, H.; Yu, Z. Z.; Koratkar, N. Fracture and Fatigue in Graphene Nanocomposites. *Small* **2010,** *6*, 179–183.
10. Ramanathan, T.; Abdala, A. A.; Stankovich, S.; Dikin, D. A.; Herrera-Alonso, M.; Piner, R. D.; Adamson, D. H.; Schniepp, H. C.; Chen, X.; Ruoff, R. S. Functionalized Graphene Sheets for Polymer Nanocomposites. *Nat. Nanotechnol.* **2008,** *3*, 327–331.
11. Stankovich, S.; Dikin, D. A.; Dommett, G. H. B.; Kohlhaas, K. M.; Zimney, E. J.; Stach, E. A.; Piner, R. D.; Nguyen, S. B. T.; Ruoff, R. S. Graphene-Based Composite Materials. *Nature* **2006,** *442*, 282–286.
12. Riley, F. L. Silicon Nitride and Related Materials. *J. Am. Ceram. Soc.* **2000,** *83*, 245–265.
13. Hyuga, H.; Jones, M. I.; Hirao, K.; Yamauchi, Y. Fabrication and Mechanical Properties of Si_3N_4/Carbon Fiber Composites with Aligned Microstructure Produced by a Seeding and Extrusion Method. *J. Am. Ceram. Soc.* **2004,** *87*, 894–899.
14. Zhan, G. D.; Kuntz, J. D.; Wan, J.; Mukherjee, A. K. Single-Wall Carbon Nanotubes as Attractive Toughening Agents in Alumina-Based Nanocomposites. *Nat. Mater.* **2002,** *2*, 38–42.
15. Zhang, T.; Kumari, L.; Du, G. H.; Li, W. Z.; Wang, Q. W.; Balani, K.; Agarwal, A. Mechanical Properties of Carbon Nanotube–Alumina Nanocomposites Synthesized by Chemical Vapor Deposition and Spark Plasma Sintering. *Compos. Part A* **2009,** *40*, 86–93.
16. Zhang, P.; Hu, P.; Zhang, X.; Han, J.; Meng, S. Processing and Characterization of ZrB_2-SiC_W Ultra-High Temperature Ceramics. *J. Alloys Compd.* **2009,** *472*, 358–362.
17. Zhang, X.; Xu, L.; Du, S.; Han, W.; Han, J. Crack-Healing Behavior of Zirconium Diboride Composite Reinforced with Silicon Carbide Whiskers. *Scripta Mater.* **2008,** *59*, 1222–1225.
18. Jeong, H.; Lee, Y. P.; Jin, M. H.; Kim, E. S.; Bae, J. J.; Lee, Y. H. Thermal Stability of Graphite Oxide. *Chem. Phys. Lett.* **2009,** *470*, 255–258.
19. Sigmund, W.; Bell, N.; Bergström, L. Novel Powder-Processing Methods for Advanced Ceramics. *J. Am. Ceram. Soc.* **2000,** *83*, 1557–1574.
20. Poyato, R.; Vasiliev, A. L.; Padture, N. P.; Tanaka, H. Aqueous Colloidal Processing of Single-Wall Carbon Nanotubes and Their Composites with Ceramics. *Nanotechnology* **2006,** *17*, 1770–1777.
21. Sun, J.; Gao, L.; Li, W. Colloidal Processing of Carbon Nanotube/Alumina Composites. *Chem. Mater.* **2002,** *14*, 5169–5172.
22. Blanch, A. J.; Lenehan, C. E.; Quinton, J. S. Optimizing Surfactant Concentrations for Dispersion of Single-Walled Carbon Nanotubes in Aqueous Solution. *J. Phys. Chem. B* **2010,** *114*, 9805–9811.
23. Corral, E. L.; Cesarano, J.; Shyam, A.; Lara-Curzio, E.; Bell, N.; Stuecker, J.; Perry, N.; Di Prima, M.; Munir, Z.; Garay, J..; *et al.* Engineered Nanostructures for Multifunctional Single-Walled Carbon Nanotube Reinforced Silicon Nitride Nanocomposites. *J. Am. Ceram. Soc.* **2008,** *91*, 3129–3137.
24. Schniepp, H. C.; Li, J. L.; McAllister, M. J.; Sai, H.; Herrera-Alonso, M.; Adamson, D. H.; Prud'homme, R. K.; Car, R.; Saville, D. A.; Aksay, I. A. Functionalized Single Graphene Sheets Derived from Splitting Graphite Oxide. *J. Phys. Chem. B* **2006,** *110*, 8535–8539.
25. Rafiee, J.; Rafiee, M. A.; Yu, Z.-Z.; Koratkar, N. Superhydrophobic to Superhydrophilic Wetting Control in Graphene Films. *Adv. Mater.* **2010,** *22*, 2151–2154.

26. Vadukumpully, S.; Paul, J.; Valiyaveettil, S. Cationic Surfactant Mediated Exfoliation of Graphite into Graphene Flakes. *Carbon* **2009,** *47*, 3288–3294.
27. Munir, Z. A.; Anselmi-Tamburini, U.; Ohyanagi, M. The Effect of Electric Field and Pressure on the Synthesis and Consolidation of Materials: A Review of the Spark Plasma Sintering Method. *J. Mater. Sci.* **2006,** *41*, 763–777.
28. Garay, J. E. Current-Activated, Pressure-Assisted Densification of Materials. *Annu. Rev. Mater. Res.* **2010,** *40*, 445–468.
29. Hulbert, D. M.; Jiang, D.; Dudina, D. V.; Mukherjee, A. K. The Synthesis and Consolidation of Hard Materials by Spark Plasma Sintering. *Int. J. Refract. Met. Hard Mater.* **2009,** *27*, 367–375.
30. Vasylkiv, O.; Borodianska, H.; Sakka, Y. Nanoreactor Engineering and SPS Densification of Multimetal Oxide Ceramic Nanopowders. *J. Eur. Ceram. Soc.* **2009,** *28*, 919–927.
31. Casolco, S. R.; Xu, J.; Garay, J. E. Transparent/Translucent Polycrystalline Nanostructured Yttria Stabilized Zirconia with Varying Colors. *Scripta Mater.* **2008,** *58*, 516–519.
32. Zhan, G. D.; Mukherjee, A. K. Carbon Nanotube Reinforced Alumina-Based Ceramics with Novel Mechanical, Electrical, and Thermal Properties. *Int. J. Appl. Ceram. Technol.* **2004,** *1*, 161–171.
33. Dusza, J.; Blugan, G.; Morgiel, J.; Kuebler, J.; Inam, F.; Peijs, T.; Reece, M. J.; Puchy, V. Hot Pressed and Spark Plasma Sintered Zirconia/Carbon Nanofiber Composites. *J. Eur. Ceram. Soc.* **2009,** *29*, 3177–3184.
34. Estili, M.; Takagi, K.; Kawasaki, A. Multiwalled Carbon Nanotubes as a Unique Agent To Fabricate Nanostructure-Controlled Functionally Graded Alumina Ceramics. *Scripta Mater.* **2008,** *59*, 703–705.
35. Balazsi, C.; Shen, Z.; Konya, Z.; Kasztovszky, Z.; Weber, F.; Vertesy, Z.; Biro, L. P.; Kiricsi, I.; Arato, P. Processing of Carbon Nanotube Reinforced Silicon Nitride Composites by Spark Plasma Sintering. *Compos. Sci. Technol.* **2005,** *65*, 727–733.
36. Anstis, G. R.; Chantikul, P.; Lawn, B. R.; Marshall, D. B. A Critical Evaluation of Indentation Techniques for Measuring Fracture Toughness: I, Direct Crack Measurements. *J. Am. Ceram. Soc.* **1981,** *64*, 533–538.
37. Dresselhaus, M. S.; Jorio, A.; Hofmann, M.; Dresselhaus, G. Perspectives on Carbon Nanotubes and Graphene Raman Spectroscopy. *Nano Lett.* **2010,** *10*, 751–758.